Journal of Volcanology and Geothermal Research 419 (2021) 107371

Contents lists available at ScienceDirect

Journal of Volcanology and Geothermal Research

journal homepage: www.elsevier.com/locate/jvolgeores

Development of magmatic topography through repeated stochastic intrusions

Daniel O'Hara [a,b,*], Nathaniel Klema [a], Leif Karlstrom [a]

[a] Department of Earth Sciences, University of Oregon, 100 Cascade Hall, 1272 University of Oregon, Eugene, OR 97403, United States of America
[b] Department of Geography, Vrije Universiteit Brussel, Pleinlann 2, 1050 Brussels, Belgium

ARTICLE INFO

Article history:
Received 3 March 2021
Received in revised form 30 July 2021
Accepted 5 August 2021
Available online 9 August 2021

Keywords:
Magma chambers
Intrusive magmatism
Stochastic processes
Numerical modeling
Landscape evolution
Plate flexure

ABSTRACT

Transcrustal magma transport systems reflect accumulation of small-volume intrusions over long timescales, transiently altering the thermal, mechanical, and compositional states of the crust. The long-term impact of such repeated and spatially-distributed intrusive magmatism on surface topography remains relatively unexplored. Here, we investigate the development of topography associated with multiple generations of intrusions within the shallow to mid-crust. Expanding a single-intrusion elastic deformation model to regional scales, we determine surface signatures associated with stochastically-emplaced magmatic bodies with different spatial distributions. We find that mean intrusion radius-to-depth ratios control whether intrusions contribute more to regional crustal thickening or local topographic relief. For intrusions emplaced randomly in space following a Poisson distribution, surface topography is well-approximated by flexure of a thin elastic plate of constant effective thickness subject to basal forcing. However, we find that spatial overlap between intrusions at depth significantly limits the amount of information encoded in topography. We end by discussing how topography generated by magmatic intrusions fits into more general landscape evolution that includes climate-driven erosion, and categorize a range of previously-studied intrusive systems according to their topographic expression and predicted long-term landscape impact.

1. Introduction

Volcanic physiographic provinces are a primary expression of mantle melting and magma transport. On the surface, volcanism generates landforms over a range of scales that are subsequently degraded through chemical and physical weathering (e.g., Hayes et al., 2002; Ferrier et al., 2013; McGuire et al., 2014). This impacts hydrology and landscape evolution over thousands to millions of years (e.g., Jefferson et al., 2010); for example, mafic volcanic rocks contribute 20–35% of the modern global CO2 silicate weathering flux despite occupying ~6% of Earth's land surface (Dessert et al., 2003; Hartmann and Moosdorf, 2012; Börker et al., 2019). But it is currently unknown how the topographic form of volcanic provinces relates to the time-evolving dynamics of deeper magmatism.

Within the crust, magmatic plumbing systems are expansive (Cashman and Giordano, 2014), storing anywhere between ~2 and > 100 times the amount of magma that extrudes on the surface (White et al., 2006; Morriss et al., 2020). Magmatic systems are transcrustal (e.g., Cashman et al., 2017; Sparks et al., 2019), likely exhibiting tiered zones containing crystal mush and distributed pockets of magma that form a time-evolving transport network between the mantle source and the surface (e.g., Samrock et al., 2018; Schmidt et al., 2008; Trevino & Miller, 2021). Such systems probably grow through incremental assembly of smaller-scale bodies (e.g., Annen et al., 2015; de Saint-Blanquat et al., 2006), and although eruptions seem to occur with a magnitude-frequency distribution (Pyle, 1995) it is unclear whether intrusions follow similar temporal statistics.

The spatial distribution of volcanic topography provides an important constraint on characteristics of the underlying magmatic structure. Volcanic vent distributions have received the most attention in this regard, reflecting the long-term history of both mantle magma sources (e.g., Kiyosugi et al., 2010; Till et al., 2019) and magma-tectonic stresses (e.g., Maccaferri et al., 2014; Toprak, 1998). Vents in monogenetic fields are often dispersed, sometimes following a Poisson spatial distribution (Baloga et al., 2007) unless structurally-controlled by faults (Connor and Hill, 1995). Conversely, long-lived polygenetic centers have more clustered vent distributions (Rowland, 1996; Kervyn et al., 2009; Karlstrom et al., 2015), suggesting focusing of rising magma within the crust. Although it is widely recognized that intruded volumes greatly exceed eruptions, the surface impact of intrusions is rarely studied, except on the largest of scales (e.g., Lee et al., 2013).

* Corresponding author at: Department of Earth Sciences, University of Oregon, 100 Cascade Hall, 1272 University of Oregon, Eugene, OR 97403, United States of America.
E-mail address: Daniel.OHara@vub.be (D. O'Hara).

https://doi.org/10.1016/j.jvolgeores.2021.107371
0377-0273/

A key obstacle in the way of understanding smaller scale magmatic topography, whether it be from surface vent distributions or intrusions, is lack of constraints on the patterns of magma transport on timescales of 10–100 s kyr. Models therefore play an important role in hypothesis testing, although the extreme range of magmatic length and timescales poses a substantial challenge that has yet to be overcome. Studies investigating the long-term thermal and mechanical evolution of crustal magmatic systems typically isolate a process of interest, making assumptions about the geometry of intrusion distributions, rheology and structure of the crust, and transport mechanics (e.g., Annen and Sparks, 2002; Dufek and Bergantz, 2005; Jackson et al., 2018). Crustal-scale models often assume a fluid (or visco-plastic, Keller et al., 2013; Colón et al., 2018) response of crustal rocks to magma intrusion, enabling treatment of the long-time and large-scale dynamics.

While viscoelastic and viscoplastic models are likely required to understand the full spectrum of magmatic deformation, elastic models of shallow single intrusions regularly see success in modeling deformation associated with active systems (e.g., Anderson et al., 2015; Castro et al., 2016; Parks et al., 2015) as well as exhumed laccoliths (e.g., Pollard and Johnson, 1973; Michaut, 2011). It is reasonable to hypothesize that the shallow crustal response to episodic intrusions will be largely elastic, even as cooling intrusions warm the crust and shallow the brittle-ductile transition (Karakas et al., 2017; Karlstrom et al., 2017). Indeed, the generic topographic form of polygenetic edifices is well modeled by surface displacement associated with repeated dilation in a homogenous elastic half space (Cosburn and Roy, 2020), and 10 kyr patterns of uplift in volcanic provinces have been approximated as elastic deformation around inflating intrusions (e.g., Singer et al., 2018).

Here, we focus solely on the impacts of stochastic intrusive magmatism on landscape scales, modeled as episodes of elastic deformation as a baseline for identifying controls on topographic form in long-lived volcanic provinces. Although an end-member both in the spectrum of magmatic landscape construction and in the context of intrusion mechanics, this framework allows us to quantitatively examine a number of questions that are relevant for magmatic topography generally. What is the topographic consequence of emplacing many generations of small-scale intrusions within the crust, as implied by the incremental input model of transcrustal magmatism? What can the surface tell us about the spatial and geometric distributions of intrusions at depth? Do these intrusions contribute only to topographic relief, crustal thickening, or a combination of both?

We address these questions by applying single-intrusion elastic deformation models stochastically at regional scales, determining the extent to which magmatic bodies of varying sizes, depths, and spatial distributions leave a surficial fingerprint. We then parameterize these results using a thin plate flexure model to gain insight on how surface characteristics relate to the distribution of intrusions at depth, and explore the extent to which clustering of intrusions represents information loss irrecoverable from topography. Our results suggest a basic framework with which to study topography associated with intrusive magmatism.

2. Methods

We study the effects of various intrusion sizes and depths on the transient evolution of topography and crustal thickening by focusing only on surficial displacement associated with multiple isolated intrusions and ignoring erosion. Below, we describe the numerical model setup and suite of model parameters explored.

2.1. Stochastic intrusion model

Processes associated with crustal magmatic emplacement are multifaceted (e.g., Tibaldi, 2015). The thermomechanical response of the crust to magmatic intrusions varies as a function of depth, temperature field, and crustal heterogeneity, and is further influenced by the geochemical evolution of magma associated with differentiation, rejuvenation, and assimilation of wall rock (e.g., Dufek and Bergantz, 2005; Annen et al., 2006; Rivalta et al., 2015).

We ignore many of these complexities and focus on a mechanical model that considers only the elastic crustal response to magmatism in the shallow crust. We assume the crust has homogeneous properties, and simulate the transient evolution of regional-scale magmatism by randomly sampling intrusion parameters from prior spatial distributions, tracking both surface displacements and cumulative intrusion thicknesses.

2.1.1. Topography from a single intrusion

Surface deformation from single magmatic intrusions in an elastic half space depend principally on intrusion radius (R) and depth (d). For example, geodetic studies often model deep ($R \ll d$) active intrusions using an inflating point source (i.e., the 'Mogi' model; Mogi, 1958) or spherical cavity (e.g., McTigue, 1987) within the crust; whereas models based on shallow ($R \gg d$) intrusions typically consider crustal flexure with a thin-plate model that neglects horizontal deformation (e.g., Pollard and Johnson, 1973; Galland and Scheibert, 2013). We use a model that approximates both end-member regimes in the $R - d$ parameter space: the vertical deformation (w) associated with pressurization of a penny-shaped crack in an elastic half space (Fialko et al., 2001),

$$w(r) = \frac{2(1-\nu)\Delta P R}{\mu} \int_0^\infty \left[\left(1 + \xi \frac{d'}{R}\right)\Phi(\xi) + \xi \frac{d'}{R}\,\Psi(\xi) \right] e^{-\frac{\xi d'}{R}} J_0(\xi r)\, d\xi, \quad (1)$$

where $r = \sqrt{(x-x_0)^2 + (y-y_0)^2}$ are radial coordinates from the intrusion center (x_0, y_0), x and y are Cartesian coordinates, ν and μ are the Poisson's ratio and shear modulus of the crust, and ΔP is the magma overpressure. We assume constant ν, μ, and ΔP values of 0.35, 20 GPa, and 40 MPa, respectively, acknowledging that there is variability in all of these parameters (particularly overpressure). J_0 is a Bessel function of the first kind, order zero, Φ and Ψ are image functions applied to iteratively satisfy free surface and crack plane boundary conditions (Fialko et al., 2001).

The penny-shaped crack inflation model assumes a flat free surface. Such an assumption is not strictly valid within the framework of our model, where generations of intrusions generate non-flat surface topography, which generate deviatoric stresses at depth (e.g., Maccaferri et al., 2011). One solution to this is to account for topography directly within the governing equations (e.g, McTigue and Stein, 1984). However, this complicates the model and is computationally expensive. A second, simpler approach is to adjust the depth of the intrusion to account for overlying regional relief. Williams and Wadge (1998) found, for the inflating point-source model, that this adjustment is equivalent to altering the governing equations to account for topography. Here, we follow this approach and calculate d' as the depth of the intrusion corrected to account for overlying topography (z):

$$d' = d + z(r = 0) - \min(z). \quad (2)$$

To analyze the connections between intrusions and surface displacements, we also model intrusion thicknesses. For simplicity, we parameterize the complicated algebraic expression for intrusion thickness from Eq. (1) as the semi-minor axis of an axisymmetric ellipsoidal body of radius R. The volume of the ellipsoid is assumed to be the volume change (ΔV) associated with the pressurized crack (Fialko et al., 2001):

$$\Delta V = \frac{4\pi R^3 (1-\nu)\Delta P}{\mu} \int_0^\infty \Phi(\xi) J_0(\xi) d\xi. \quad (3)$$

This approximation simplifies the geometry of the intrusion, although we note that it becomes progressively more inaccurate as R/d

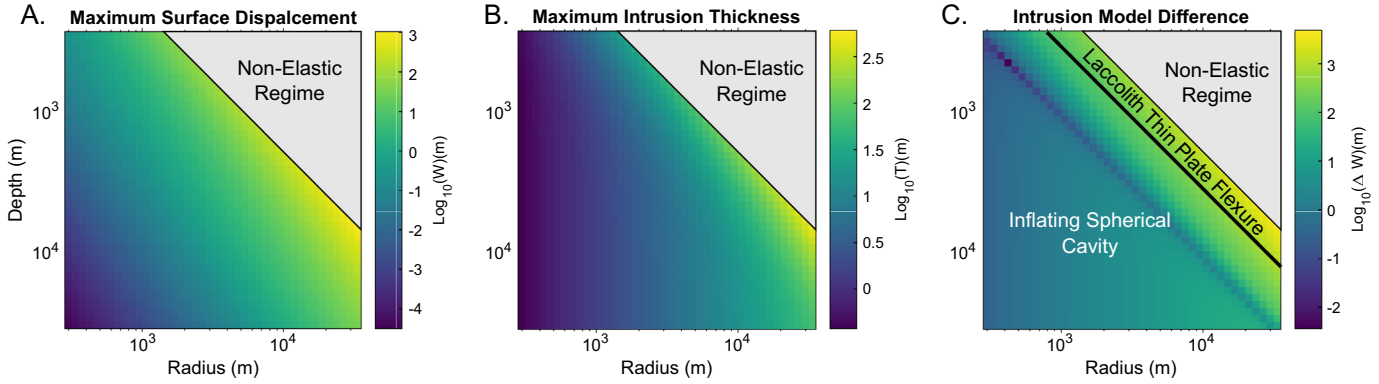

Fig. 1. Stochastic model intrusion radius-depth ($\boldsymbol{R-d}$) parameter space using the pressurized penny-shaped crack displacement model (Fialko et al., 2001). **A:** Maximum surface displacement. **B:** Maximum intrusion thickness. **C:** Displacement difference between pressurized penny-shaped crack and typical inflating point source (McTigue, 1987) and thin-plate flexure (Galland and Scheibert, 2013) models. Black line represents parameter values that create equal maximum surface displacements between inflating spherical cavity and thin-plate flexure models. Non-elastic regime defines the $\boldsymbol{R/d}$ limitation of the inflating penny-shaped crack model (~5.6; Fialko et al., 2001).

increases (Cervelli, 2013). Below, we contextualize this model within the framework of end-member models for magmatic intrusions.

Fig. 1.A–B shows maximum surface displacements and maximum thicknesses of single intrusions within our explored $R-d$ parameter space. Fig. 1.C shows the difference in maximum surface displacements between the pressurized penny-shaped crack, inflating point source, and thin-plate flexure models (Δw). Overall differences between these models are small (<1 m), except for the largest intrusive bodies within the shallow regime, where the intrusion lateral dimension is much larger than its depth and the pressured-crack model becomes inappropriate.

2.2. Topography from many intrusions

We explore the effects of repeated intrusions over extended time by stochastically sampling the $R-d$ associated with a single intrusion and correcting surface deformation from prior intrusions using Eq. (2). For all models, we intrude magmatic bodies into a periodic spatial grid that has a length of 63.75 km in both x and y directions, and a grid resolution of 250 m. We sample from an intrusion $R-d$ parameter space ranging ~316–31,600 m (Fig. 2), which falls within the size distributions of mapped plutonic bodies (Cruden et al., 2018). For consistency across models, we intrude a total magmatic volume of 2000 km^3, within the

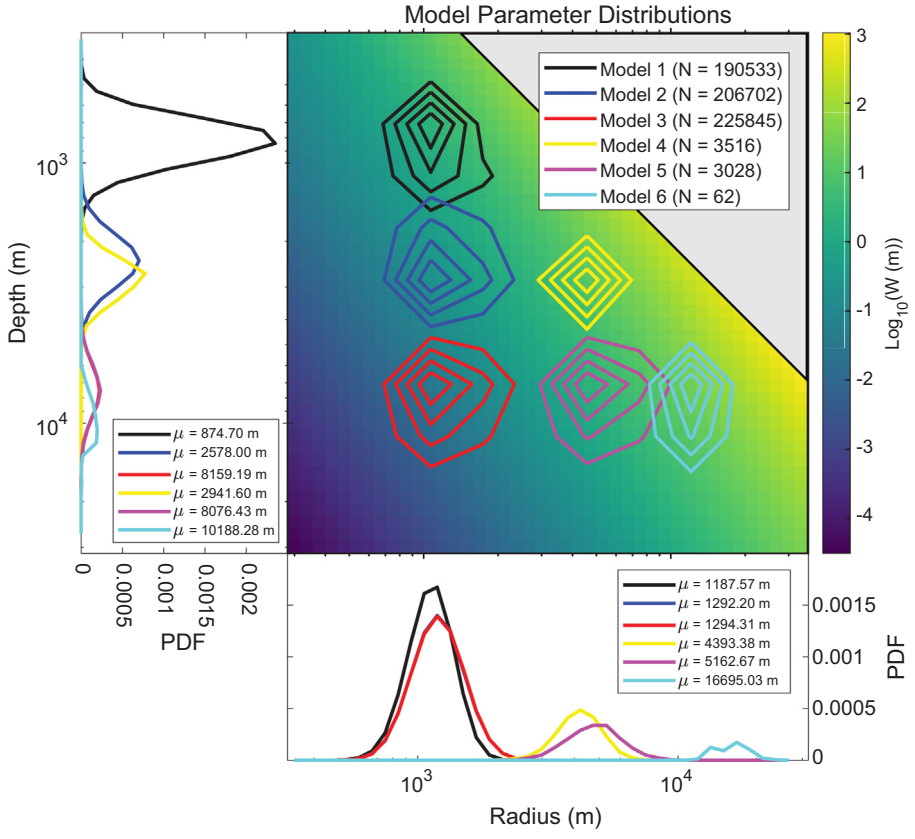

Fig. 2. Sampled $\boldsymbol{R-d}$ distributions for Poisson spatially-distributed models. Colored lines represent 20% contours of sampled values for each model; inset gives the total number of samples (N). Bottom and left panels show the probability density functions (PDFs) of sampled radius (bottom) and depth (left) values for each model; insets give the mean sampled value ($\boldsymbol{\mu}$).

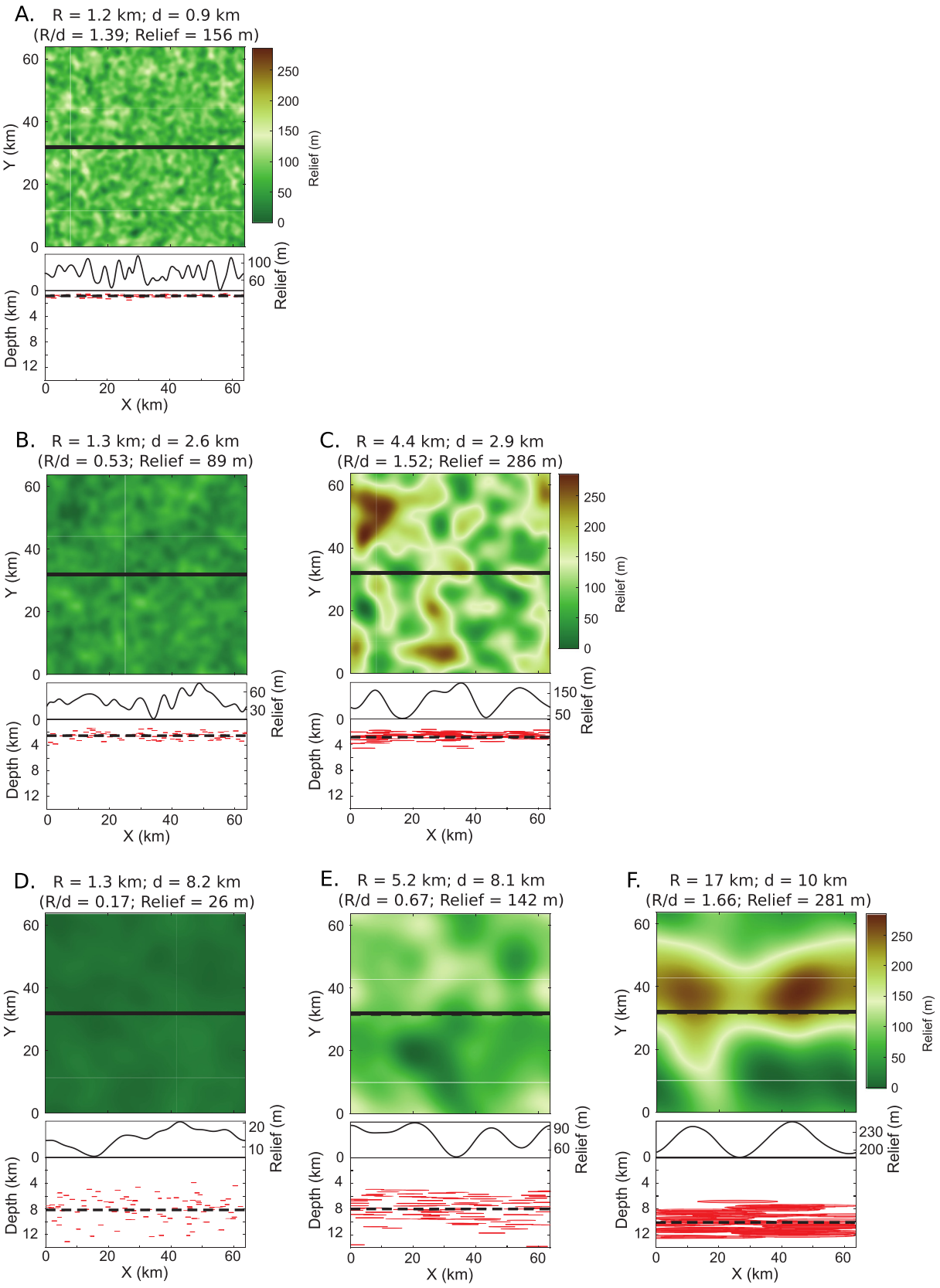

Fig. 3. Poisson spatial distribution model topography, ordered according to ***R/d*** as in Fig. 2. Top panels show model relief. Bottom panels show cross-sections of both topography and crust through the black lines of top panels. Red ellipses signify locations of intrusions within the cross-section, with thicknesses vertically-exaggerated by 10%. Black-dashed lines show mean intrusion depth. Mass balance results in mean topography of ~500 m across all models shown here.

estimated ranges of exposed plutonic provinces (de Saint Blanquat et al., 2011). Given our spatial grid size, this volume should generate ~500 m of mean elevation in all models. We assume a normal bivariate distribution of R and d with standard deviations ranging ~200–2400 m and no covariance between the two parameters. Across all models, the maximum sampled R/d ratio is ~1.9, well within the appropriate parameter space of the penny-shaped crack model (Fialko et al., 2001).

We test the impact of intrusion spatial distributions on topographic form by assuming intrusions have nearest-neighbor distances that follow a Poisson (memory-less) distribution, and determine intrusion locations by randomly sampling a uniform distribution in both the x and y directions. Thus, we model a system of nearly equal-sized intrusions at nearly equal depths that are randomly distributed in map view. Fig. 3 shows the final model topography and crustal cross-section of emplaced intrusions for six simulations that span the model parameter space. Although Eq. (1) is linear, our correction for depth in Eq. (2) breaks linearity as an intrusion's surface deformation becomes dependent on the relief formed by previous intrusions. We examine the impact of this dependence on our model results with a sensitivity test using a small number of intrusions for each of the sampled mean intrusion parameters (Appendix A). Overall, we find reordering is a negligible effect, varying topography by ±0.4% of the reported values.

3. Results

Our models generate distributed topography on a range of scales. Shallow, small-radius intrusions create shorter wavelength topography. As intrusion depth increases relative to radius, longer-wavelength features become more apparent, with the R/d ratio setting overall amplitude (Fig. 3). Within all models, the mean elevation of topography is ~500 m, as expected from the volumetric input of magma into the crust and the spatial dimensions of our grid. Below, we describe our analysis and results of the model topography.

3.1. Model topographic analysis

We analyze the effect of intrusion geometric and spatial distributions on topography using two metrics. We first assess the overall elevation increase of each model by calculating maximum and mean elevations. We then compare the volume of topographic relief to the volume of crustal thickening within each model that does not generate relief. The volume of relief (V_r) is defined as the volume in excess of the minimum topography in the model domain defined by $X_d = Y_d =$ 63,750 m,

$$V_r = \int_0^{X_d}\int_0^{Y_d} z\, dy\, dx - V_T, \tag{4}$$

where $V_T = \min(z)\, X_d\, Y_d$ is the volume of uniform crustal thickening. We then define a parameter ζ as the ratio of relief to thickening

$$\zeta = \frac{V_r}{V_T}, \tag{5}$$

which provides a useful metric for determining whether intrusion distributions contribute more to local topography ($\zeta > 1$, relief generation dominates) or regional ($\zeta < 1$, crustal thickening dominates) quasi-uniform uplift. By analogy to magmatic intrusive/extrusive ratios generally, ζ measures the extent to which magma transport is measurable at the surface or is hidden from direct observation.

However, Eq. (5) does not provide insight into the physical controls on topographic relief. We strive to understand the relationship between buried loads at depth (such as intrusions) and topography with a reduced order model of our simulations, seeking to parameterize the stochastic intrusion models as a thin plate with effective elastic thickness T_e to a vertical force of magmatic origin at its base. Thin plate elasticity can be applied in cases where deformation (w) is primarily vertical and both deformation and the effective elastic thickness of the plate are small compared to its lateral dimensions (e.g., Watts, 2001). For simplicity, we assume no lateral forces acting upon the plate and that deflections are small enough that in-plane tensile stresses can be ignored (Timoshenko and Woinowsky-Krieger, 1959). Assuming the density of air is negligible, the 2D flexure equation is (Wessel, 1996)

$$D\nabla^4 w(x,y) = q_p(x,y) - \rho_m g w(x,y), \tag{6}$$

where q_p is the pressure at the base of the plate, g is acceleration due to gravity, and ρ_m is the density of magma, such that the final term of Eq. (6) represents a restoring force that scales with maximum displacement. D is the flexural rigidity, defined as

$$D = \frac{ET_e^3}{12(1-\nu^2)}, \tag{7}$$

with Young's modulus E. For consistency between models, we use a Young's modulus value $E = 2\mu(1+\nu) = 5.4 \times 10^{10}$ Pa (Turcotte and Schubert, 2010). Eq. (6) is conveniently treated in the spectral domain, for which we define the 2D Fourier and inverse Fourier transform pair of a signal (f) as

$$\overline{f}(k_x,k_y) = \int_{-\infty}^{\infty}\int_{-\infty}^{\infty} f(x,y) e^{-2\pi i\left(xk_x+yk_y\right)} dxdy, \tag{8}$$

$$f(x,y) = \int_{-\infty}^{\infty}\int_{-\infty}^{\infty} \overline{f}(k_x,k_y) e^{2\pi i\left(xk_x+yk_y\right)} dk_x dk_y, \tag{9}$$

with wave numbers k_x and k_y in the x and y direction, respectively. Rearranging Eq. (6), we Fourier transform the flexure equation to derive an algebraic expression for surface displacement as a function of wavenumber for the plate

$$\overline{w}(k_x,k_y) = \phi(\boldsymbol{k})\overline{q}(k_x,k_y), \tag{10}$$

where $\boldsymbol{k}$ is the radial wave number $\left(\boldsymbol{k} = \sqrt{k_x^2+k_y^2}\right)$ and $\phi(\boldsymbol{k})$ is the isostatic response function (Walcott, 1970), defined as

$$\phi = \frac{1}{2\pi\boldsymbol{k}^4 D + g\rho_m}. \tag{11}$$

Eq. (11) predicts the mechanical response of a plate with rigidity D to loading at different length scales. For example, short-wavelength (large $\boldsymbol{k}$) perturbations cause ϕ to approach 0, in which case the plate appears rigid and no displacement occurs. Under long-wavelength loading the plate is weak and the load will be compensated as $1/g\rho_m$ (Airy isostacy). In the transitional waveband between these end-member responses elastic behavior dominates and the plate acts as a linear filter, distributing the load across a characteristic "flexural wavelength" λ_C defined as (Watts, 2001)

$$\lambda_C = 2\pi\left(\frac{D}{\rho_m g}\right)^{\frac{1}{4}}. \tag{12}$$

We apply Eq. (11) to determine an effective elastic thickness for our stochastic intrusion models as the effective depth of our intrusion distribution, with which we can calculate the admittance between intrusion thickness and relief (Krishna, 1996). A best-fitting elastic thickness for each model is found through grid search over the range ~32 − 50,000 m. The lower limit of our parameter search falls within the range of depths explored previously for shallow rhyolitic intrusions (Castro et al., 2016). For each thickness, we calculate ϕ using Eq. (11), then determine the misfit (δ) between ϕ and the admittance as

$$\delta = \sqrt{\sum_{i=-K_x}^{K_x} \sum_{j=-K_y}^{K_y} \left(\mathrm{Re}\left(\frac{\overline{z}(k_i, k_j)}{\overline{\tau}(k_i, k_j)} \right) - \phi(\boldsymbol{k}(k_i, k_j))\Gamma \right)^2}, \quad (13)$$

where $\overline{z}$ and $\overline{\tau}$ are the spectral components of total relief and intrusion thickness, i and j are counters of k_x and k_y, and K_x and K_y are Nyquist wavenumbers in the k_x and k_y directions. Γ is a conversion factor between pressure and thickness, which parameterizes the loading of a thin plate associated with a Poisson-distributed sequence of intrusions. For simplicity, we assume Γ is a constant value of $\rho_m g$, with $\rho_m = 2800$ kg/m^3, though in reality Γ likely depends on intrusion depths and radii. Furthermore, we calculate δ using average ϕ and admittance values within binned wavenumbers for computational efficiency.

When applied to noisy natural systems, data is often scaled by the complex conjugate of topography within Eq. (13) (e.g., McKenzie and Bowin, 1976; Watts, 1978). In these settings, the phase of the admittance (ϕ_α) is analyzed as $e^{2i\phi_{\alpha(\boldsymbol{k})}} = \alpha(\boldsymbol{k})/\alpha^*(\boldsymbol{k})$, where $\alpha(\boldsymbol{k})$ is the admittance and $\alpha^*(\boldsymbol{k})$ is its complex conjugate (Watts, 2001). If surface displacements are perfectly aligned with the source of basal pressure, as is the case in this study, the phase is expected to be zero, however this might not always be the case in settings where magma chambers are offset from overlying volcanic edifices representing deposits and lateral mass transport (Lerner et al., 2020).

3.2. The topographic signatures of magmatism

Within our model set, intrusion geometry distributions correspond to variability in the overall height and relief of topography, ranging ~500–650 m and ~20–250 m, respectively. The intrusion mean radius-to-depth ratio (R/d) exerts a clear control on these metrics, as increasing R/d ratios generate both higher topography and higher-relief features (Fig. 4). This trend between elevation and model intrusion parameters extends further to the amount of relief versus crustal thickening generated by intrusions (ζ; Eq. (5)). The ratio ζ is less than 1 for all models (Fig. 5), demonstrating that intrusions contribute most to crustal thickening. Furthermore, R/d values influence the distribution of volume, with largest R/d values creating more topographic relief. An expectation of this relationship is that ζ should go to 0 as R/d approaches 0. Using this assumption, we derive a best-fitting linear relationship between R/d and ζ (Fig. 5, red line).

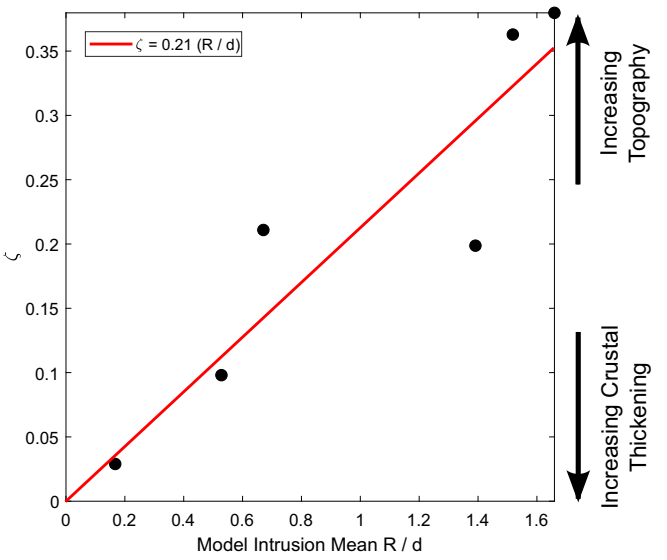

Fig. 5. Volume of topographic relief divided by volume of crustal thickening associated with stochastic intrusions ($\boldsymbol{\zeta}$; Eq. (5)), ordered by mean model intrusion radius-to-depth ratio for Poisson spatial intrusion distributions. Red line is best-fitting linear fit of data.

Further insight into controls on topography comes from a constant thickness thin plate model. Fig. 6.A shows the grid search δ values (Eq. (13)) over the analyzed elastic plate thickness parameter space, ordered by mean stochastic model intrusion depth on the y-axis. In all cases, despite a range of intrusion depths, we find a reasonably well-fitting elastic plate to predict topography. While much effort has gone into understanding the physical meaning of effective elastic thickness in the lithosphere, it can be broadly thought of as the depth to which elastic processes must dominate to produce observed deformation in a coherent layer (Burov and Diament, 1995). Under the thin-plate approximation, this implies a stress field that varies linearly with both surface curvature and depth. In our model space with purely mechanical inputs, T_e likely represents a point of spatial averaging above which

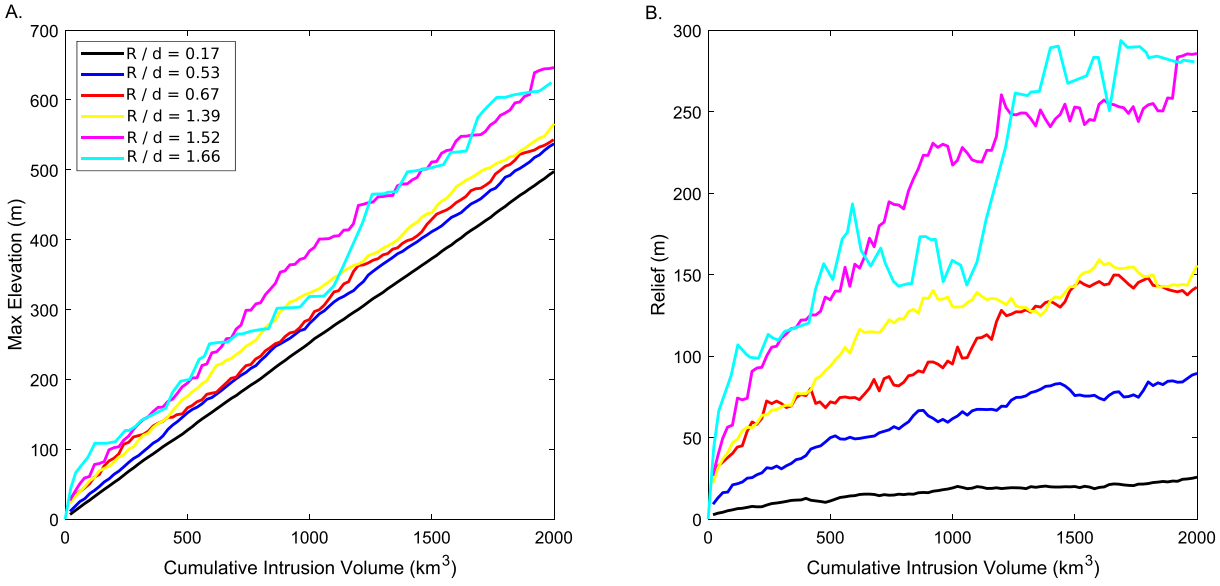

Fig. 4. (**A**) Maximum elevation and (**B**) relief of model topography as a function of cumulative intrusive volume for Poisson spatial intrusion distribution models, illustrating our stochastic simulation procedure. Colors correspond to model parameters presented in legend, showing increasing topography with increasing ***R*/*d***.

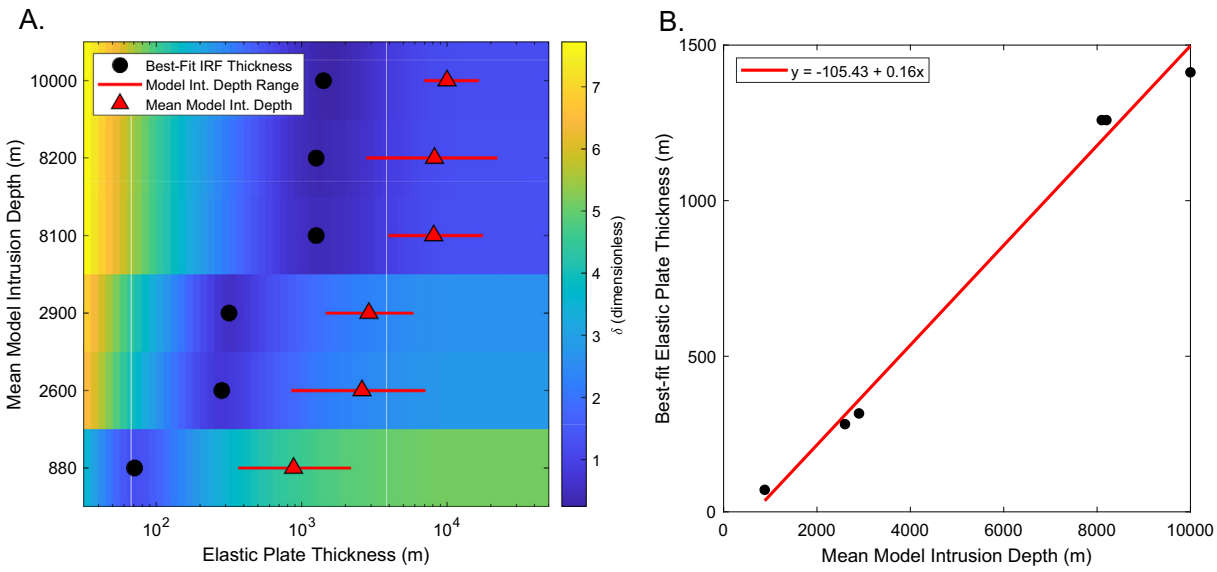

Fig. 6. Elastic plate flexure model fits to Poisson spatial intrusion distribution models. **A:** Misfit (δ; Eq. (13)) between scaled isostatic response functions (ϕ; Eq. (11)) and surface-thickness transfer functions. X-axis is elastic plate thickness, Y-axis is individual Poisson distribution models, ordered by mean model intrusion depth. Black dots are lowest misfit values for each model. Red lines show range of sampled model intrusion depths, with red triangles corresponding to the mean value. **B:** Best-fitting elastic plate thicknesses as a function the corresponding mean model intrusion depth. Red line shows linear regression of values, suggesting best-fitting thin plate thickness are ≤ ~16% of mean model intrusion depths. R^2 value of linear fit is 0.99.

such a stress field is approximated, and below which stresses more strongly vary with proximity to local intrusions amounting to a breakdown in the thin-plate assumptions. Nonetheless, mean intrusion depth sets the scale for relief: Fig. 6.B suggests stochastic model mean intrusion depths and best-fitting plate thicknesses are linearly related.

Fig. 7 provides context for how these factors can influence our results by plotting the $z - \tau$ admittance for each model as a function of wavelength, ordered by mean model intrusion depth. In all models, short-wavelength (~10^2 m) admittance is well fit by the onset of flexural response predicted by the thin plate isostatic response function. Moderate wavelengths (~10^3 m) are less well-fit, indicating that a constant thickness elastic plate does not approximate the full model spectrum. These deviations are most pronounced in model runs with shallower intrusions, suggesting that misfit may result in part from a breakdown in the assumptions of our thin-plate model that occurs when vertical deformation is on the same order as T_e. In the case of large plate deflections, a considerable amount of total strain energy goes into lateral deformation along the midplane of the plate (assumed to be unstressed under small deflections), and higher-order terms in the governing equations can no longer be ignored (Ribe, 1982). This introduces complex non-linearity under which less vertical deformation is expected (Timoshenko and Woinowsky-Krieger, 1959). While this behavior highlights the limitations of our simplified framework, the realignment of model admittance values with the isostatic response function at approximately the flexural wavelength of the best-fitting elastic plate (Fig. 7, red-dashed lines), as well as the consistent relationship between mean intrusion depth and best-fitting elastic thickness (Fig. 6.B), suggests that thin-plate elasticity provides a simple proxy for topography associated with distributed intrusions at a range of depths in the upper crust.

4. Discussion

Volcanic terrain forms through the dynamic coupling between volcanic, tectonic, and erosive processes, generating spatially- and temporally-overlapping signatures of construction and degradation. Deconvolving these signals is a significant challenge but, as has been demonstrated in other tectonic settings (e.g., Kirby and Whipple, 2001), could provide new insight into the structure of crustal-magmatic systems (e.g., O'Hara et al., 2020), and their coupling to Earth surface processes (e.g., Lee et al., 2013). Here, we discuss broader implications of our study for volcanology and geomorphology, and provide examples of where our approach might be applicable.

4.1. Topographic expressions of magmatism

Volcanic landforms encompass a range of shapes and sizes, having planform areas that span ~9 orders of magnitude (Karlstrom et al., 2018). Volcanic deposition can generate relief on regional scales by mantling pre-existing surfaces, while also constructing (or in some cases removing) topography on the local scale (e.g., Branca et al., 2011). Subsurface magmatic intrusions also contribute to edifice growth (e.g., Annen et al., 2001; Biggs et al., 2010; Cosburn and Roy, 2020) and can generate regional-scale uplift over long timescales through the accumulation of magma within the upper crust (e.g., Pollard and Johnson, 1973; Perkins et al., 2016b).

Our study analyzes the regional-scale surface response to elastic deformation associated with multiple stochastically-placed magmatic intrusions within the upper-crust, which parallels observations of active systems on long timescales. For example, gravity (Trevino et al., 2021) and paleo shoreline data (Singer et al., 2018) of the Laguna del Maule volcanic field in Chile suggest multiple shallow intrusions within an ~600 km^2 area that contributed to at least ~60 m of uplift during the Holocene. While not directly comparable to our idealized model that does not include eruptive deposits or time, the distributed Laguna del Maule deformation is well-modeled by landscape-scale uplift from a distribution of intrusions in a dominantly elastic host.

Evidence for cumulative thickening of the crust from magmatism, as predicted by generations of intrusions with small R/d in our model, is also common. Deep crustal zenoliths (Chin et al., 2012), bulk strain estimates in exhumed arcs (Cao et al., 2016), and global evidence for volcanic arc front migration associated with geochemical proxies (Karlstrom et al., 2014), all point to pervasive magmatic crustal thickening. Our model demonstrates that intrusions, even within the mid- to upper-crust, can manifest as a spatially-uniform uplift rate associated with mantle-derived magma influx.

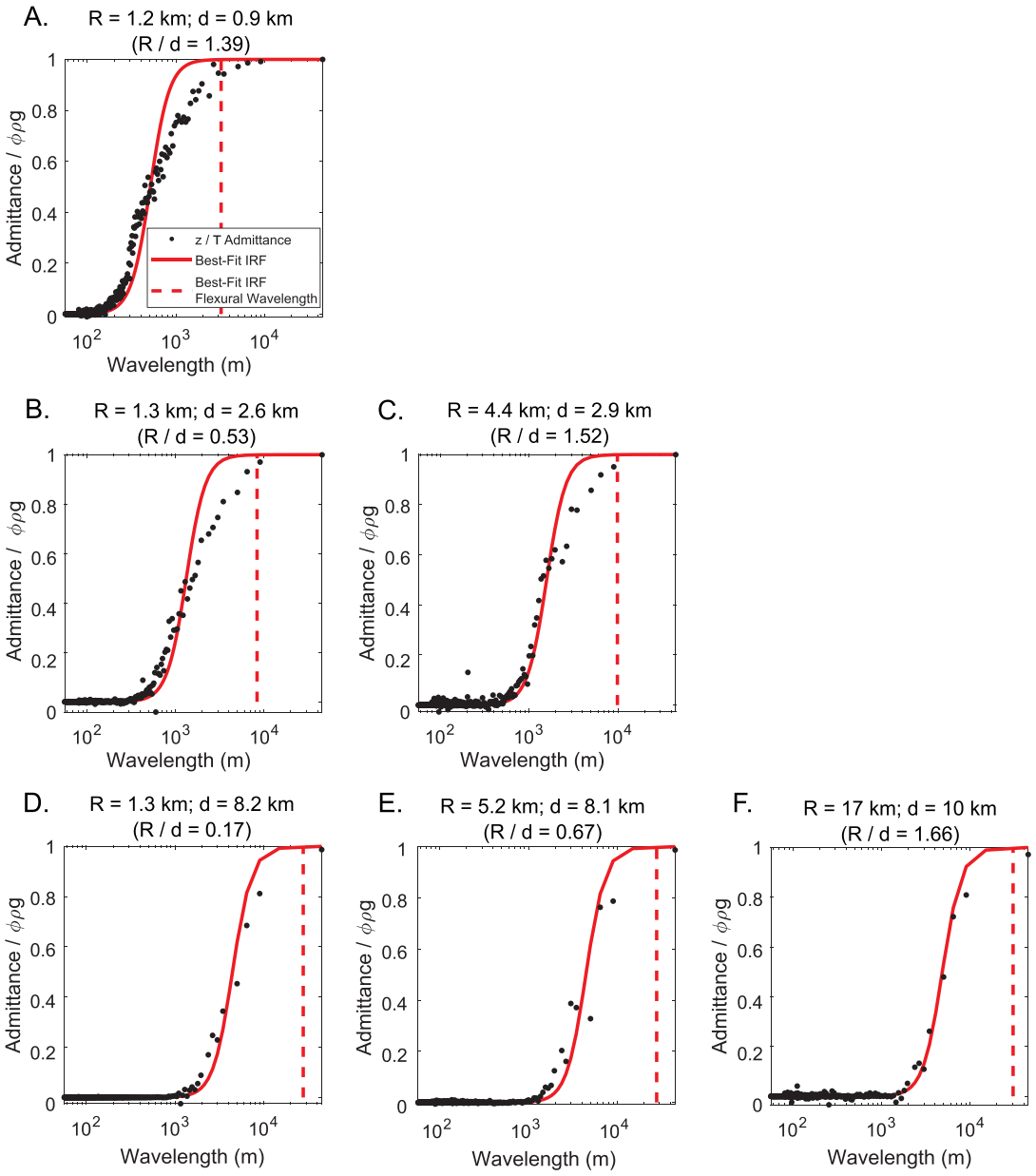

Fig. 7. Spectral admittance between surface topography $\boldsymbol{z}$ and intrusion thickness $\boldsymbol{\tau}$ (black dots) and best-fitting isostatic response (red lines) as a function of wavelength for each Poisson spatial intrusion distribution model, ordered by mean model intrusion depth. Red-dashed lines correspond to the flexural wavelength of the best-fitting elastic plate thickness ($\boldsymbol{\lambda_c}$; Eq. (12)). Plots ordered according to $\boldsymbol{R/d}$ as in Fig. 2.

4.2. The role of intrusion spatial distribution

The Poisson distribution is one of many possibilities for the spatial arrangement of magmatic intrusions. Long-lived volcanic centers (e.g., Mt. Mazama; Karlstrom et al., 2015) as well as exposed plutons (e.g., Sierra Nevada; Ardill et al., 2018) often exhibit clustered spatial distributions of magmatic features. To test the surficial response to such focused magmatism, we explore a second set of models that follow a Gaussian spatial distribution. We use the same *R* and *d* parameter distributions as the first model set (Fig. 2), and assume intrusions emplace as bivariate normal distributions in both the *x* and *y* directions with 10 km standard deviations, no covariance between the two directions, and mean locations that are centered on the model grid. This set of models thus simulates clustered intrusions of nearly-equal radius and depth within the crust. Fig. 8. A–C shows the final model topography and crustal cross section for three *R* – *d* end-member simulations that follow this intrusion spatial distribution.

Rather than dispersed topographic features generated by Poisson distributions, the Gaussian models create a single, near-axisymmetric landform with overall heights that are approximately three times higher than the Poisson distribution models (Fig. 8.A–C). The impact of these models on the volume distribution of topography is also apparent in our local relief – crustal distribution ratio (ζ, Eq. (5)), with values ranging ~7–2000.

These results imply that intrusion spatial distribution is a dominating factor for the long-term generation of topography. While mean intrusion *R* and *d* set the range of displacement during each intrusion, it is the accumulation of spatially-focused magmatic bodies over long timescales that sets relief. This is also evident in the Poisson spatial distribution models, with larger intrusions having a higher degree of spatial overlap and contributing to the formation of local topography. Cosburn and Roy (2020) analyzed the ability of spatially-focused dikes to emulate stratovolcano morphologies, finding that such models can recreate volcano topography and provide information on the subsurface

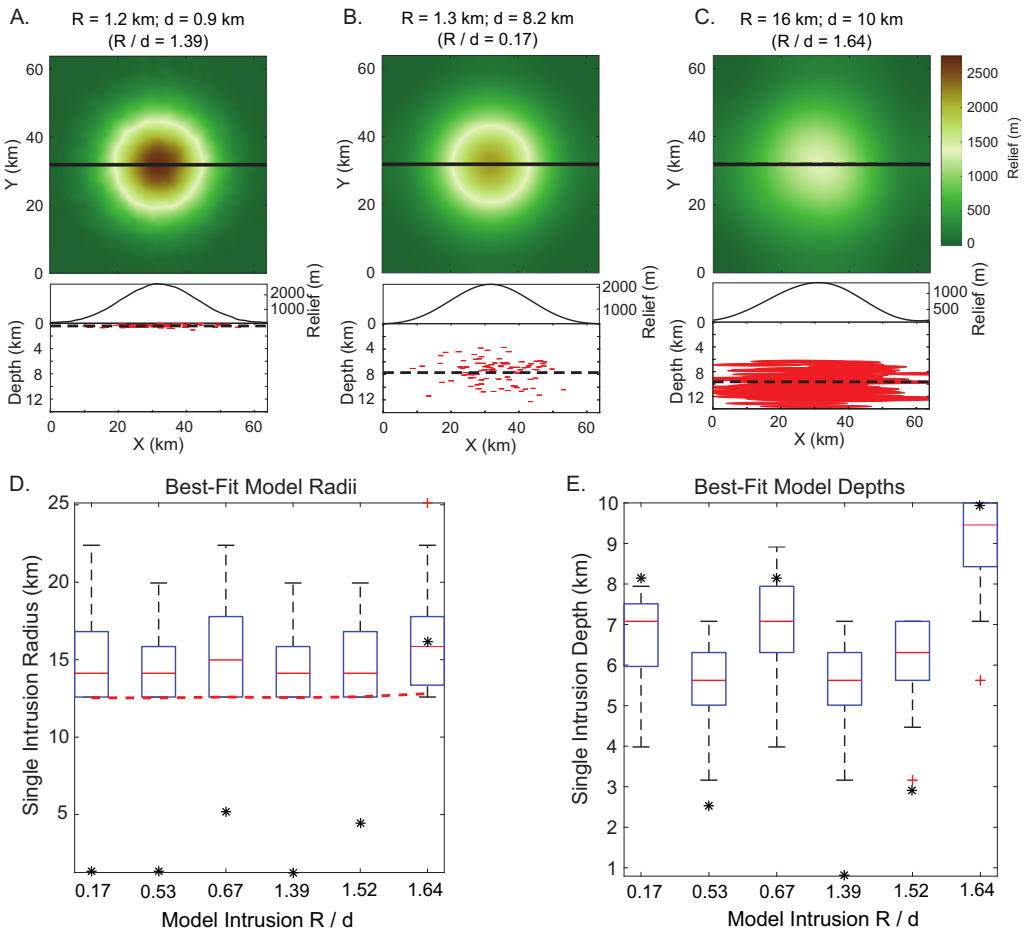

Fig. 8. A–C: Gaussian spatial distribution model topography, ordered by ***d***. Top panels show model relief. Bottom panels show cross-sections of both topography and crust through the black lines of top panels. Red ellipses signify locations of intrusions within the cross-section, with thicknesses vertically-exaggerated by 10%. Black-dashed lines show mean intrusion depth. **D–E:** Box-and-whisker plots of best-fitting single-intrusion model parameters to the Gaussian spatial intrusion distribution models for the intrusion overpressure 10–200 MPa values. X-axes are stochastic model mean ***R***/***d*** values, Y-axes are best-fitting single-intrusion parameter values. Black stars correspond to mean stochastic model parameter values. **D:** Intrusion radii. **E:** Intrusion depths.

magma structure. Here, we show a similar impact on the growth of volcanic landforms through a series of horizontal pressurized crack models.

Finally, we explore the amount of information that can be gained from the axisymmetric topography generated by our Gaussian spatial distribution models using a simple approach that is common in studies of landforms associated with shallow intrusions (e.g., Pollard and Johnson, 1973; Goulty and Schofield, 2008; Galland and Scheibert, 2013). Assuming model topography was generated by a single inflating crack (Eq. (1)), we find the best-fit intrusion parameters that match the observed pattern of deformation by performing a grid search of the same $R - d$ intrusive ranges as our stochastic models (~316–31,600 m). We compare our models to the single-intrusion fit by calculating the least squares error between the single-intrusion and stochastic intrusion model topography. We also assume effective magma overpressure is unknown, and find the best-fitting $R - d$ parameters for overpressure values ranging 10 − 200 MPa.

Best-fitting single intrusions that match the topography of our Gaussian spatial distribution models significantly differ from the model intrusion input parameters. Fig. 8.D–E shows the best-fitting single intrusion parameters for the 10–200 MPa overpressure values as a set of box-and-whisker plots for each model, ordered by stochastic model intrusion R/d ratios. Overall, we observe no consistent trend between stochastic model mean and best-fitting single intrusion parameters. However, we find that the minimum best-fitting single-intrusion radii are well-constrained by the average distance between intrusion locations and the center of the grid (Fig. 8.D, red-dashed line). This indicates that the primary magmatic input expressed in the topography is the lateral extent of intrusion distributions. As intrusive bodies become more clustered, horizontal overlap within the crustal column translates to surface deformation and thus presents a loss of information. Although this approach of constraining surface deformation as a single intrusion is commonly employed, especially accurate where both vertical and horizontal deformation can be estimated (e.g., Dzurisin et al., 2009; Parks et al., 2015), our analysis suggests that single-intrusion models of incrementally constructed shallow plutonic bodies (laccoliths and shallow sills, e.g., Pollard and Johnson, 1973; Galland and Scheibert, 2013) are non-uniquely constrained by vertical displacement data alone.

4.3. Landscape evolution forced by magmatic intrusions

We have focused here on intrusive magmatism and its role on topographic development. In real landscapes, climate-driven erosion redistributes mass along the Earth's surface and landscape evolution reflects a competition between a variety of erosion mechanisms and uplift generated by tectonic or magmatic processes. While outside the scope of our study to model the full range of processes involved in volcanic landscape evolution, our model suggests that stochastically-emplaced intrusions can have a large impact on topographic development. There are two ways this can happen. If the ratio of magmatic topographic relief versus crustal thickening (ζ, Eq. (5)) is much smaller than unity,

intrusions will contribute to a regionally uniform background uplift rate (commonly associated solely with tectonics in non-volcanic settings, e.g., Whipple and Tucker, 1999; Willett, 1999). Alternatively, as ζ approaches or exceeds unity, magmatic intrusions create more localized topography.

This localized and transient uplift can have long-lasting impacts on eroding landscapes. Assuming a surface dominantly eroded by fluvial incision in channels and linear diffusion on ridges (soil creep), O'Hara et al. (2019) analyzed the effects of single localized uplift perturbations on topographic evolution, finding three regimes which contribute to increasing landscape disruption as perturbations become more significant compared to initial topography that guides surface processes. Interpreting such perturbations as arising from magmatic intrusions, we can relate our purely constructional models to more general landscape evolution by assessing the topographic impact of intrusions compared to pre-existing topography. We do this in a relatively qualitative manner here, by predicting the impact of known intrusion episodes that are distinguishable from any concurrent extrusive magmatic construction.

In the regime diagram of O'Hara et al. (2019), two nondimensional numbers related to the geometry of the localized uplift and pre-existing landscape govern transient surface response (Fig. 9.A). The first number, β, compares maximum intrusion surface displacement to the overlying topographic relief. When surface displacement is small compared to topography ($\beta \lesssim 1$; Fig. 9.B, Regime 1) intrusions generate very little surface disruption on regional scales, forming small convexities within river channels and surrounding terrain. A possible example of this process is the rapid, low relief-generating uplift often associated with approximately years-long volcanic deformation from isolated intrusive episodes (assuming such deformation is permanent). In this regime, it is not likely that magmatic uplift will permanently change pre-exiting topography, although there may be a transient response in the form of knickpoints, landslides, or other small-scale adjustments. The purely constructional model developed here is unlikely to be a good descriptor of landscape evolution in this regime.

The second nondimensional number, η, compares the size of the intrusion to the pre-exiting fluvial drainage basin size (i.e., lateral wavelength of topography before the intrusion), measuring relative rates of landscape adjustment by bedrock erosion. When $\beta > 1$, but intrusions are much smaller than pre-existing landforms ($\eta \ll 1$; Fig. 9.B, Regime 2), landscape disruption may include beheaded river channels and internally-drained basins. This disruption is not permanent, and in the absence of other forcing, the landscape may eventually relax to a pre-intrusion state. However, the imprint of transient uplift is long-lasting if lateral reconfiguration of river networks occurs in response to the intrusion (O'Hara et al., 2019).

Finally, as β exceeds 1 and η approaches or exceeds 1, intrusion size becomes larger than pre-existing topography and the surface will experience a high degree of disruption (Fig. 9.B, Regime 3). The landform will become the dominant topographic feature of the landscape, forming a long-term drainage divide that forces permanent channel network reconfiguration in the surrounding landscape. Regime 3 represents magmatically-dominated landscape evolution, of the kind modeled here.

Following the framework of O'Hara et al. (2019), we attempt to quantify the $\beta - \eta$ values for select locations where intrusive magmatism is a known contributor to surface uplift (Fig. 9.B). Our aim in placing this set of intrusions spanning a range of sizes and timescales on a single landscape regime diagram is to identify phenomenological similarities in their likely long-term impact, rather than precise predictions. The presently-active uplift episode on the western flank of South Sister (OR, U.S.; Wicks et al., 2002; Dzurisin et al., 2009), and episodic uplift associated with the Socorro magma body (NM, U.S.; Finnegan and Pritchard, 2009), likely represent Regime 1 perturbations. In these regions, recorded cumulative uplift is much lower than surrounding topography (i.e., $\beta < 1$), with η values varying based on the comparison topographic wavelength of the uplifted region. Conversely, the Pleistocene – present construction of Lazufre (Argentina-Chile border) and the Altiplano-Puna Volcanic Complex (Argentina-Chile-Bolivia border) fall within Regime 3. Both locations have generated high-relief landforms compared to surrounding topography, and have altered drainage patterns throughout their lifespan (Perkins et al., 2016a). Another example of a Regime 3 perturbation is the Oligocene-age laccoliths of the Henry Mountains (Utah, U.S.; Gilbert, 1877). Despite continued Basin-and-Range extension and re-working of regional drainage networks on the Colorado Plateau (e.g., Cather et al., 2008; Murray et al., 2016), these km-scale features have remained dominant, long-standing landforms that have altered local channel configurations (Cook et al., 2009).

Regimes 1 and 3 have relatively clearly-defined examples; Regime 2 is not as easily identifiable as it represents a transient step between short-term deformation and long-term dominant landform generation.

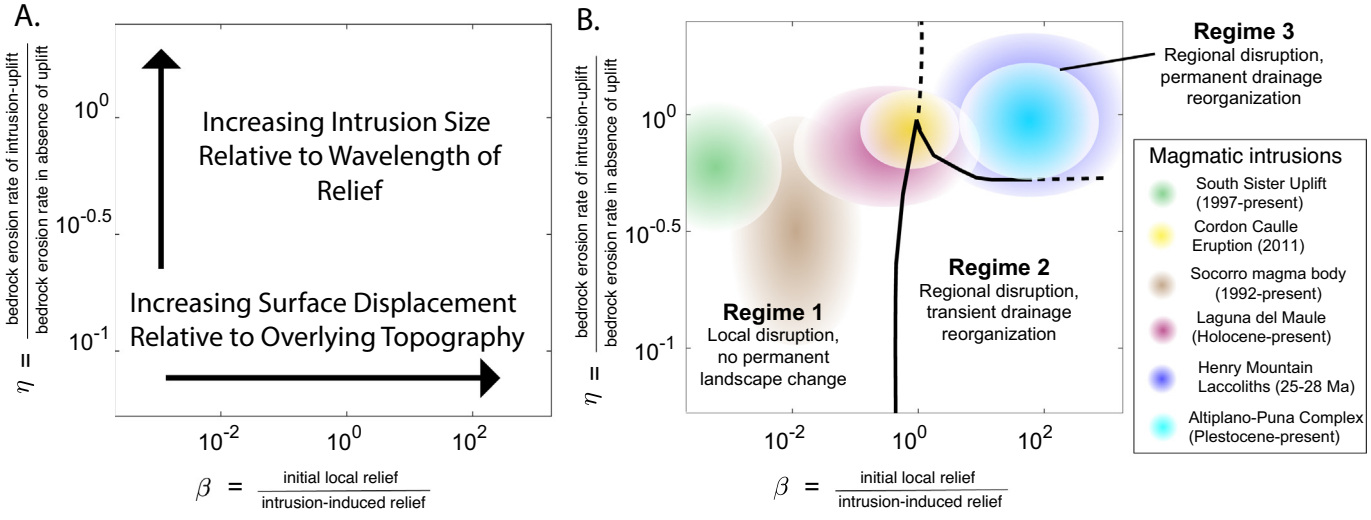

Fig. 9. Regime diagram for magmatic intrusion impacts on landscape evolution, modified from O'Hara et al. (2019). **A:** Intrusion parameter effects on nondimensional numbers measuring the geometry of intrusion relative to pre-existing topography. **B:** Landscape evolution regimes, boundaries from the parameter study of O'Hara et al. (2019). Colors correspond to estimated $\beta - \eta$ ranges for a number of known magmatic intrusive episodes, described in the text. Uncertainty in the nondimensional numbers comes from unknown previous landscape form (for older intrusions such as the Henry Mountains) and uncertain erosional response (for younger intrusions).

However, two locations that might span all three regimes include the 2011 uplift of Cordon Caulle (Chile), and the Holocene uplift at Laguna del Maule (Chile). At Cordon Caulle, rapid inflation of a shallow laccolith in 2011 generated ~200 m of uplift on the northwestern flank of a larger volcano (Castro et al., 2016), generating nearly-equal relief to the surrounding terrain on a lengthscale similar to the main volcano. Similarly, intrusion-related uplift throughout the Holocene on the southeast region of Laguna del Maule contributed to ~60 m of relief (Singer et al., 2018). Although this cumulative uplift is smaller than surrounding relief generated by near-contemporaneous rhyolitic flows, pre-flow topography may be on similar, if not lower, scales to the inflation.

Of course, volcanic landscape evolution involves a wide range of impacts from eruptive deposits as well as intrusions. In addition to altering topographic relief, deposition of effusive lava changes the hydrologic regime of the near surface (Jefferson et al., 2010; Jefferson et al., 2014), and modulates the mechanisms and rates of erosion (e.g., Pierson and Major, 2014). The magnitude-frequency dependence of volcanism/landform production may determine the pattern and magnitude of erosion in volcanic settings (Karlstrom et al., 2018). We see great potential in further work towards a process-based understanding of volcanic landscape evolution to uncover surface signatures of time-varying mantle flux.

5. Conclusion

We study the impact of regional-scale intrusive magmatism on development of topography in volcanic settings. By modeling stochastic intrusions in the shallow to mid-crust, we simulate the long-term topographic response to episodic crustal magma transport over a range of lengthscales. We show that generation of topographic relief versus crustal thickening varies as a function of mean intrusion parameters, providing a simple proxy for analyzing crustal magmatism from topography. Furthermore, we find that the topographic response to distributed magmatism can be approximated using a thin plate flexure model, providing a predictive tool that can be easily extended to include gravity and structural constraints. Despite information loss due to overlapping intrusions, we find that a range of topography can catalog the spatial extent of intrusive bodies and thus informs the geometry of the shallow crustal transport network. We postulate that combining our results with topographic modeling of landforms in volcanic provinces to separate signatures of magmatic, tectonic, and climate will provide new avenues towards estimating long-term crustal magma flux and magmatic system geometry from the surface.

Declaration of Competing Interest

The authors declare that they have no known competing financial interests or personal relationships that could have appeared to influence the work reported in this paper.

Acknowledgements

We thank Jonathan Perkins and an anonymous reviewer for their insight and suggestions, which enhanced the quality of this manuscript. We thank Paul Richardson and Joshua J. Roering for discussions. This work was supported by NSF GRF 1309047 to D.O. and NSF CAREER 1848554 to L.K.

Appendix A. Model sensitivity

Topographic correction to models of intrusion sequences introduces a non-linear dependence of surface uplift on the relative ordering of intrusions. We test the effect of intrusion sequencing on topography through a small sensitivity test. We generate five intrusions for each mean intrusion radius and depth analyzed in the main text (Fig. 2). Intrusion radii are set to the mean value, and depths are randomly generated around the mean, assuming a normal distribution within our parameter space. We then calculate surface deformation using the penny-shaped crack model (Eq. (1)), generating topography for every possible permutation of intrusion orders (120 combinations). Spatially, we set the intrusions in a cross-pattern, with one intrusion in the center and the other four surrounding it on all sides. We assume the distance between the center intrusion and the others is the half-radius of the intrusion, explicitly testing the depth correction (Eq. (2)) by allowing intrusions to overlap.

Afterwards, we calculate maximum elevation sensitivity ($\dot{z}_{max}(p)$) as a percentage for each permutation p:

$$\dot{z}_{max}(p) = \left(\frac{z_{max}(p)}{\bar{z}_{max}} - 1\right) * 100, \tag{A.1}$$

where $z_{max}(p)$ is the maximum elevation of topography generated by the permutation, and $\bar{z}_{max}$ is the average maximum elevation of all permutations within the set of intrusions. Fig. A1 shows the results of this analysis as a set of box-and-whisker plots for each model intrusion mean R/d. Although the variation in maximum topography increases as R/d becomes larger, topography varies by only $\pm 0.4\%$ at the largest sampled mean R/d. This suggests the non-linearity introduced by our depth correction in Eq. (2) is negligible for the range of intrusion parameters explored here.

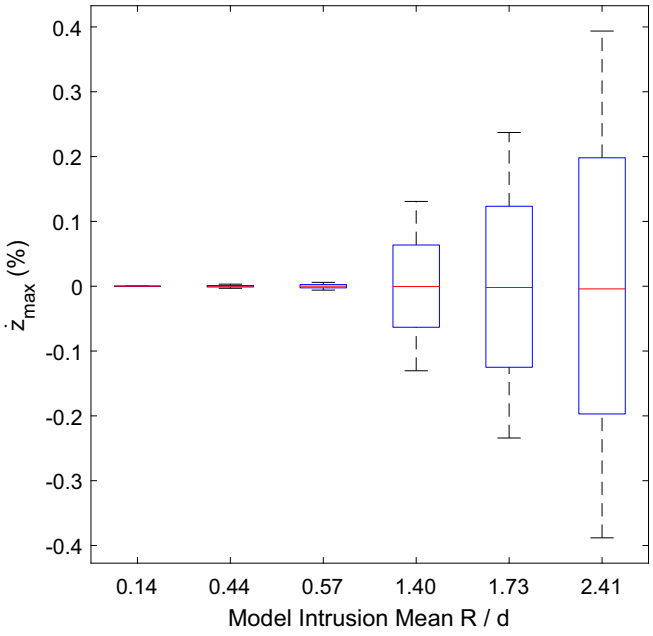

Fig. A1. Model topography sensitivity analysis (Eq. (A.1)), ordered by mean model intrusion ***R/d***.

References

Anderson, K.R., Poland, M.P., Johnson, J.H., Miklius, A., 2015. Episodic deflation–inflation events at kīlauea volcano and implications for the shallow magma system. Geophys. Monograph Series 208, 229–250. https://doi.org/10.1002/9781118872079.ch11.

Annen, C., Sparks, R.S.J., 2002. Effects of repetitive emplacement of basaltic intrusions on thermal evolution and melt generation in the crust. Earth Planet. Sci. Lett. 203, 937–955. https://doi.org/10.1016/S0012-821X(02)00929-9.

Annen, C., Lénat, J.F., Provost, A., 2001. The long-term growth of volcanic edifices: numerical modelling of the role of dyke intrusion and lavaa-flow emplacement. J. Volcanol. Geotherm. Res. 105, 263–289. https://doi.org/10.1016/S0377-0273(00)00257-2.

Annen, C., Blundy, J.D., Sparks, R.S.J., 2006. The genesis of intermediate and silicic magmas in deep crustal hot zones. J. Petrol. 47, 505–539. https://doi.org/10.1093/petrology/egi084.

Annen, C., Blundy, J.D., Leuthold, J., Sparks, R.S.J., 2015. Construction and evolution of igneous bodies: towards an integrated perspective of crustal magmatism. Lithos 230, 206–221. https://doi.org/10.1016/j.lithos.2015.05.008.

Ardill, K., Paterson, S., Memeti, V., 2018. Spatiotemporal magmatic focusing in upper-mid crustal plutons of the Sierra Nevada arc. Earth Planet. Sci. Lett. 498, 88–100. https://doi.org/10.1016/j.epsl.2018.06.023.

Baloga, S.M., Glaze, L.S., Bruno, B.C., 2007. Nearest-neighbor analysis of small features on Mars: applications to tumuli and rootless cones. J. Geophys.Res. E: Planets 112, 1–17. https://doi.org/10.1029/2005JE002652.

Biggs, J., Mothes, P., Ruiz, M., Amelung, F., Dixon, T.H., Baker, S., Hong, S.H., 2010. Stratovolcano growth by co-eruptive intrusion: the 2008 eruption of Tungurahua Ecuador. Geophys. Res. Lett. 37. https://doi.org/10.1029/2010GL044942.

Börker, J., Hartmann, J., Romero-Mujalli, G., Li, G., 2019. Aging of basalt volcanic systems and decreasing CO2 consumption by weathering. Earth Surf. Dynam. 7, 191–197. https://doi.org/10.5194/esurf-7-191-2019.

Branca, S., Coltelli, M., Groppelli, G., 2011. Geological evolution of a complex basaltic stratovolcano: Mount Etna, Italy. Ital. J. Geosci. 130, 306–317. https://doi.org/10.3301/IJG.2011.13.

Burov, E.B., Diament, M., 1995. The effective elastic thickness (Te) of continental lithosphere: what does it really mean? J. Geophys. Res. 100, 3905–3927. https://doi.org/10.1029/94JB02770.

Cao, W., Paterson, S., Saleeby, J., Zalunardo, S., 2016. Bulk arc strain, crustal thickening, magma emplacement, and mass balances in the Mesozoic Sierra Nevada arc. J. Struct. Geol. 84, 14–30. https://doi.org/10.1016/j.jsg.2015.11.002.

Cashman, K.V., Giordano, G., 2014. Calderas and magma reservoirs. J. Volcanol. Geotherm. Res. 288, 28–45. https://doi.org/10.1016/j.jvolgeores.2014.09.007.

Cashman, K.V., Sparks, R.S.J., Blundy, J.D., 2017. Vertically extensive and unstable magmatic systems: a unified view of igneous processes. Science, 355 https://doi.org/10.1126/science.aag3055.

Castro, J.M., Cordonnier, B., Schipper, C.I., Tuffen, H., Baumann, T.S., Feisel, Y., 2016. Rapid laccolith intrusion driven by explosive volcanic eruption. Nat. Commun. 7, 1–7. https://doi.org/10.1038/ncomms13585.

Cather, S.M., Connell, S.D., Chamberlin, R.M., McIntosh, W.C., Jones, G.E., Potochnik, A.R., Lucas, S.G., Johnson, P.S., 2008. The Chuska erg: paleogeomorphic and paleoclimatic implications of an Oligocene sand sea on the Colorado Plateau. Bull. Geol. Soc. Am. 120, 13–33. https://doi.org/10.1130/B26081.1.

Cervelli, P., 2013. Analytical expressions for deformation from an arbitrarily oriented spheroid in a half-space. AGU Fall Meeting Abstracts. 93, pp. 12–13.

Chin, E.J., Lee, C.T.A., Luffi, P., Tice, M., 2012. Deep lithospheric thickening and refertilization beneath continental arcs: case study of the P, T and compositional evolution of peridotite xenoliths from the Sierra Nevada, California. J. Petrol. 53, 477–511. https://doi.org/10.1093/petrology/egr069.

Colón, D.P., Bindeman, I.N., Wotzlaw, J.F., Christiansen, E.H., Stern, R.A., 2018. Origins and evolution of rhyolitic magmas in the central snake river plain: insights from coupled high-precision geochronology, oxygen isotope, and hafnium isotope analyses of zircon. Contrib. Mineral. Petrol. 173, 1–18. https://doi.org/10.1007/s00410-017-1437-y.

Connor, C.B., Hill, B.E., 1995. Three nonhomogeneous Poisson models for the probability of basaltic volcanism: application to the Yucca Mountain region, Nevada. J. Geophys. Res. 100. https://doi.org/10.1029/95jb01055.

Cook, K.L., Whipple, K.X., Heimsath, A.M., Hanks, T.C., 2009. Rapid incision of the Colorado River in Glen Canyon – insights from channel profiles, local incision rates, and modeling of lithologic controls. Earth Surf. Process. Landf. https://doi.org/10.1002/esp.

Cosburn, K., Roy, M., 2020. Analysing the topographic form of stratovolcanoes. J. Volcanol. Geotherm. Res. 407, 107123. https://doi.org/10.1016/j.jvolgeores.2020.107123.

Cruden, A.R., McCaffrey, K.J.W., Bunger, A.P., 2018. Geometric scaling of tabular igneous intrusions: implications for emplacement and growth. Advances in Volcanology, pp. 11–38 https://doi.org/10.1007/11157_2017_1000.

de Saint Blanquat, M., Horsman, E., Habert, G., Morgan, S., Vanderhaeghe, O., Law, R., Tikoff, B., 2011. Multiscale magmatic cyclicity, duration of pluton construction, and the paradoxical relationship between tectonism and plutonism in continental arcs. Tectonophysics 500, 20–33. https://doi.org/10.1016/j.tecto.2009.12.009.

de Saint-Blanquat, M., Habert, G., Horsman, E., Morgan, S.S., Tikoff, B., Launeau, P., Gleizes, G., 2006. Mechanisms and duration of non-tectonically assisted magma emplacement in the upper crust: The Black Mesa pluton, Henry Mountains, Utah. Tectonophysics 428, 1–31. https://doi.org/10.1016/j.tecto.2006.07.014.

Dessert, C., Dupré, B., Gaillardet, J., François, L.M., Allègre, C.J., 2003. Basalt weathering laws and the impact of basalt weathering on the global carbon cycle. Chem. Geol. 202, 257–273. https://doi.org/10.1016/j.chemgeo.2002.10.001.

Dufek, J., Bergantz, G.W., 2005. Lower crustal magma genesis and preservation: a stochastic framework for the evaluation of basalt-crust interaction. J. Petrol. 46, 2167–2195. https://doi.org/10.1093/petrology/egi049.

Dzurisin, D., Lisowski, M., Wicks, C.W., 2009. Continuing inflation at three sisters volcanic center, central oregon cascade range, USA, from GPS, leveling, and InSAR observations. Bull. Volcanol. 71, 1091–1110. https://doi.org/10.1007/s00445-009-0296-4.

Ferrier, K.L., Huppert, K.L., Perron, J.T., 2013. Climatic control of bedrock river incision. Nature 496, 206–209. https://doi.org/10.1038/nature11982.

Fialko, Y., Khazan, Y., Simons, M., 2001. Deformation due to a pressurized horizontal circular crack in an elastic half-space, with applications to volcano geodesy. Geophys. J. Int. 146, 181–190. https://doi.org/10.1046/j.1365-246X.2001.00452.x.

Finnegan, N.J., Pritchard, M.E., 2009. Magnitude and duration of surface uplift above the Socorro magma body. Geology 37, 231–234. https://doi.org/10.1130/G25132A.1.

Galland, O., Scheibert, J., 2013. Analytical model of surface uplift above axisymmetric flat-lying magma intrusions: implications for sill emplacement and geodesy. J. Volcanol. Geotherm. Res. 253, 114–130. https://doi.org/10.1016/j.jvolgeores.2012.12.006.

Gilbert, G.K., 1877. Geology of the Henry Mountains: Government Printing Office.

Goulty, N.R., Schofield, N., 2008. Implications of simple flexure theory for the formation of saucer-shaped sills. J. Struct. Geol. 30, 812–817. https://doi.org/10.1016/j.jsg.2008.04.002.

Hartmann, J., Moosdorf, N., 2012. The new global lithological map database GLiM: a representation of rock properties at the Earth surface. Geochem. Geophys. Geosyst. 13, 1–37. https://doi.org/10.1029/2012GC004370.

Hayes, S.K., Montgomery, D.R., Newhall, C.G., 2002. Fluvial sediment transport and deposition following the 1991 eruption of Mount Pinatubo. Geomorphology 45, 211–224. https://doi.org/10.1016/S0169-555X(01)00155-6.

Jackson, M.D., Blundy, J., Sparks, R.S.J., 2018. Chemical differentiation, cold storage and remobilization of magma in the Earth's crust. Nature 564, 405–409. https://doi.org/10.1038/s41586-018-0746-2.

Jefferson, A., Grant, G.E., Lewis, S.L., Lancaster, S.T., 2010. Coevolution of hydrology and topography on a basalt landscape in the Oregon Cascade Range, USA. Earth Surf. Process. Landf. 35, 803–816. https://doi.org/10.1002/esp.1976.

Jefferson, A.J., Ferrier, K.L., Perron, J.T., Ramalho, R., 2014. Controls on the hydrological and topographic evolution of shield volcanoes and Volcanic Ocean Islands. The Galapagos: A Natural Laboratory for the Earth Sciences, pp. 185–213 https://doi.org/10.1002/9781118852538.ch10.

Karakas, O., Degruyter, W., Bachmann, O., Dufek, J., 2017. Lifetime and size of shallow magma bodies controlled by crustal-scale magmatism. Nat. Geosci. 10, 446–450. https://doi.org/10.1038/ngeo2959.

Karlstrom, L., Lee, C.T.A., Manga, M., 2014. The role of magmatically driven lithospheric thickening on arc front migration. Geochem. Geophys. Geosyst. 15, 2655–2675. https://doi.org/10.1002/2014GC005355.

Karlstrom, L., Wright, H.M., Bacon, C.R., 2015. The effect of pressurized magma chamber growth on melt migration and pre-caldera vent locations through time at Mount Mazama, Crater Lake, Oregon. Earth Planet. Sci. Lett. 412, 209–219. https://doi.org/10.1016/j.epsl.2014.12.001.

Karlstrom, L., Paterson, S.R., Jellinek, A.M., 2017. A reverse energy cascade for crustal magma transport. Nat. Geosci. 10, 604–608. https://doi.org/10.1038/NGEO2982.

Karlstrom, L., Richardson, P.W., O'Hara, D., Ebmeier, S.K., 2018. Magmatic Landscape Construction. J. Geophys. Res. Earth Surf. 123, 1710–1730. https://doi.org/10.1029/2017JF004369.

Keller, T., May, D., Kaus, B., 2013. Finite-Element Modelling of Visco-Elasto-Plastic Two-Phase Flow. v. 15 p. 3275.

Kervyn, M., Ernst, G.G.J., van Wyk de Vries, B., Mathieu, L., Jacobs, P., 2009. Volcano load control on dyke propagation and vent distribution: insights from analogue modeling. J. Geophys. Res., 114 https://doi.org/10.1029/2008jb005653.

Kirby, E., Whipple, K., 2001. Quantifying differential rock-uplift rates via stream profile analysis. Geology 29, 415–418. https://doi.org/10.1130/0091-7613(2001)029<0415:QDRURV>2.0.CO;2.

Kiyosugi, K., Connor, C.B., Zhao, D., Connor, L.J., Tanaka, K., 2010. Relationships between volcano distribution, crustal structure, and P-wave tomography: an example from the Abu Monogenetic Volcano Group, SW Japan. Bull. Volcanol. 72, 331–340. https://doi.org/10.1007/s00445-009-0316-4.

Krishna, M.R., 1996. Isostatic response of the Central Indian Ridge (Western Indian Ocean) based on transfer function analysis of gravity and bathymetry data. Tectonophysics 257, 137–148. https://doi.org/10.1016/0040-1951(95)00114-x.

Lee, C.T.A., Shen, B., Slotnick, B.S., Liao, K., Dickens, G.R., Yokoyama, Y., Lenardic, A., Dasgupta, R., Jellinek, M., Lackey, J.S., Schneider, T., Tice, M.M., 2013. Continental arc-island arc fluctuations, growth of crustal carbonates, and long-term climate change. Geosphere 9, 21–36. https://doi.org/10.1130/GES00822.1.

Lerner, A.H., O'Hara, D., Karlstrom, L., Ebmeier, S.K., Anderson, K.R., Hurwitz, S., 2020. The prevalence and significance of offset magma reservoirs at arc volcanoes. Geophys. Res. Lett., 47 https://doi.org/10.1029/2020GL087856.

Maccaferri, F., Bonafede, M., Rivalta, E., 2011. A quantitative study of the mechanisms governing dike propagation, dike arrest and sill formation. J. Volcanol. Geotherm. Res. 208, 39–50. https://doi.org/10.1016/j.jvolgeores.2011.09.001.

Maccaferri, F., Rivalta, E., Keir, D., Acocella, V., 2014. Off-rift volcanism in rift zones determined by crustal unloading. Nat. Geosci. 7, 297–300. https://doi.org/10.1038/ngeo2110.

McGuire, L.A., Pelletier, J.D., Roering, J.J., 2014. Development of topographic asymmetry: Insights from dated cinder cones in the western United States. J. Geophys. Res. F: Earth Surface 119, 1725–1750. https://doi.org/10.1002/2014JF003081.

McKenzie, D., Bowin, C., 1976. The relationship between bathymetry and gravity in the Atlantic Ocean. J. Geophys. Res. 81, 1903–1915. https://doi.org/10.1029/jb081i011p01903.

McTigue, D.F., 1987. Elastic stress and deformation near a finite spherical magma body: resolution of the point source paradox. J. Geophys. Res. 92, 12931. https://doi.org/10.1029/jb092ib12p12931.

McTigue, D.F., Stein, R.S., 1984. Topographic amplification of tectonic displacement: implications for geodetic measurement of strain changes. J. Geophys. Res. 89, 1123–1131. https://doi.org/10.1029/JB089iB02p01123.

Michaut, C., 2011. Dynamics of magmatic intrusions in the upper crust: theory and applications to laccoliths on Earth and the Moon. J. Geophys. Res. 116, B05205. https://doi.org/10.1029/2010JB008108.

Mogi, K., 1958. Relations between the eruptions of various volcanoes and the deformations of the ground surfaces around them. Bull. Earthquake Res. Inst. 36, 99–134. https://doi.org/10.1016/j.epsl.2004.04.016.

Morriss, M.C., Karlstrom, L., Nasholds, M.W.M., Wolff, J.A., 2020. The chief Joseph dike swarm of the Columbia river flood basalts, and the legacy data set of William H. Taubeneck. Geosphere 16, 1793–1817. https://doi.org/10.1130/GES02173.1.

Murray, K.E., Reiners, P.W., Thomson, S.N., 2016. Rapid Pliocene-Pleistocene erosion of the Central Colorado Plateau documented by apatite thermochronology from the Henry Mountains. Geology 44, 483–486. https://doi.org/10.1130/G37733.1.

O'Hara, D., Karlstrom, L., Roering, J.J., 2019. Distributed landscape response to localized uplift and the fragility of steady states. Earth Planet. Sci. Lett. 506, 243–254. https://doi.org/10.1016/j.epsl.2018.11.006.

O'Hara, D., Karlstrom, L., Ramsey, D.W., 2020. Time-evolving surface and subsurface signatures of Quaternary volcanism in the Cascades arc. Geology https://doi.org/10.1130/g47706.1.

Parks, M.M., Moore, J.D.P., Papanikolaou, X., Biggs, J., Mather, T.A., Pyle, D.M., Raptakis, C., Paradissis, D., Hooper, A., Parsons, B., Nomikou, P., 2015. From quiescence to unrest: 20 years of satellite geodetic measurements at Santorini volcano, Greece. J. Geophys. Res. Solid Earth 120, 1309–1328. https://doi.org/10.1002/2014JB011540.

Perkins, J.P., Finnegan, N.J., Henderson, S.T., Rittenour, T.M., 2016a. Topographic constraints on magma accumulation below the actively uplifting Uturuncu and Lazufre volcanic centers in the Central Andes. Geosphere 12, 1078–1096. https://doi.org/10.1130/GES01278.1.

Perkins, J.P., Ward, K.M., De Silva, S.L., Zandt, G., Beck, S.L., Finnegan, N.J., 2016b. Surface uplift in the Central Andes driven by growth of the Altiplano Puna Magma Body. Nat. Commun. 7, 1–10. https://doi.org/10.1038/ncomms13185.

Pierson, T.C., Major, J.J., 2014. Hydrogeomorphic effects of explosive volcanic eruptions on drainage basins. Annu. Rev. Earth Planet. Sci. 42, 469–507. https://doi.org/10.1146/annurev-earth-060313-054913.

Pollard, D.D., Johnson, A.M., 1973. Mechanics of growth of some laccolithic intrusions in the Henry mountains, Utah, II. Bending and failure of overburden layers and sill formation. Tectonophysics 18, 311–354. https://doi.org/10.1016/0040-1951(73)90051-6.

Pyle, D.M., 1995. Mass and energy budgets of explosive volcanic eruptions. Geophys. Res. Lett. 22, 563–566. https://doi.org/10.1029/95GL00052.

Ribe, N.M., 1982. On the interpretation of frequency response functions for oceanic gravity and bathymetry. Geophys. J. R. Astron. Soc. 70, 273–294. https://doi.org/10.1111/j.1365-246X.1982.tb04968.x.

Rivalta, E., Taisne, B., Bunger, A.P., Katz, R.F., 2015. A review of mechanical models of dike propagation: schools of thought, results and future directions. Tectonophysics 638, 1–42. https://doi.org/10.1016/j.tecto.2014.10.003.

Rowland, S.K., 1996. Slopes, lava flow volumes, and vent distributions on Volcán Fernandina, Galápagos Islands. J. Geophys. Res. B: Solid Earth 101, 27657–27672. https://doi.org/10.1029/96jb02649.

Samrock, F., Grayver, A.V., Eysteinsson, H., Saar, M.O., 2018. Magnetotelluric image of transcrustal magmatic system beneath the Tulu Moye geothermal prospect in the Ethiopian Rift. Geophys. Res. Lett. 45, 12,847–12,855. https://doi.org/10.1029/2018GL080333.

Schmidt, M.E., Grunder, A.L., Rowe, M.C., 2008. Segmentation of the Cascade Arc as indicated by Sr and Nd isotopic variation among diverse primitive basalts. Earth Planet. Sci. Lett. 266, 166–181. https://doi.org/10.1016/j.epsl.2007.11.013.

Singer, B.S., Le Mével, H., Licciardi, J.M., Córdova, L., Tikoff, B., Garibaldi, N., Andersen, N.L., Diefenbach, A.K., Feigl, K.L., 2018. Geomorphic expression of rapid Holocene silicic magma reservoir growth beneath Laguna del Maule, Chile. Sci. Adv. 4, 1–11. https://doi.org/10.1126/sciadv.aat1513.

Sparks, R.S.J., Annen, C., Blundy, J.D., Cashman, K.V., Rust, A.C., Jackson, M.D., 2019. Formation and dynamics of magma reservoirs: Philosophical transactions of the Royal Society A. Math. Phys. Eng. Sci. 377. https://doi.org/10.1098/rsta.2018.0019.

Tibaldi, A., 2015. Structure of volcano plumbing systems: a review of multi-parametric effects. J. Volcanol. Geotherm. Res. 298, 85–135. https://doi.org/10.1016/j.jvolgeores.2015.03.023.

Till, C.B., Kent, A.J.R., Abers, G.A., Janiszewski, H.A., Gaherty, J.B., Pitcher, B.W., 2019. The causes of spatiotemporal variations in erupted fluxes and compositions along a volcanic arc. Nat. Commun. 10, 1350. https://doi.org/10.1038/s41467-019-09113-0.

Timoshenko, S.P., Woinowsky-Krieger, S., 1959. Theory of Plates and Shells: New York. McGraw-Hill Education.

Toprak, V., 1998. Vent distribution and its relation to regional tectonics, Cappadocian Volcanics, Turkey. J. Volcanol. Geotherm. Res. 85, 55–67. https://doi.org/10.1016/S0377-0273(98)00049-3.

Trevino, S.F., Miller, C.A., Tikoff, B., Fournier, D., Singer, B.S., 2021. Multiple, coeval silicic magma storage domains beneath the Laguna Del Maule volcanic field inferred from gravity investigations. J. Geophys. Res. Solid Earth https://doi.org/10.1029/2020jb020850.

Turcotte, D.L., Schubert, G., 2010. Geodynamics: New York. Cambridge University Press.

Walcott, R.I., 1970. Isostatic response to loading of the crust in Canada. Can. J. Earth Sci. 7, 716–727. https://doi.org/10.1139/e70-070.

Watts, A.B., 1978. An analysis of isostasy in the world's oceans; 1. Hawaiian-Emperor Seamount Chain. J. Geophys. Res. 83, 5989–6004. https://doi.org/10.1029/JB083iB12p05989.

Watts, A.B., 2001. Isostasy and Flexure of the Lithosphere. Cambridge University Press.

Wessel, P., 1996. Analytical solutions for 3-D flexural deformation of semi-infinite elastic plates. Geophys. J. Int. 124, 907–918. https://doi.org/10.1111/j.1365-246X.1996.tb05644.x.

Whipple, K.X., Tucker, G.E., 1999. Dynamics of the stream-power river incision model: implications for height limits of mountain ranges, landscape response timescales, and research needs. J. Geophys. Res. Solid Earth 104, 17661–17674. https://doi.org/10.1029/1999jb900120.

White, S.M., Crisp, J.A., Spera, F.J., 2006. Long-term volumetric eruption rates and magma budgets. Geochem. Geophys. Geosyst. 7. https://doi.org/10.1029/2005GC001002.

Wicks, C.W., Dzurisin, D., Ingebritsen, S., Thatcher, W., Lu, Z., Iverson, J., 2002. Magmatic activity beneath the quiescent Three Sisters volcanic center, central Oregon Cascade Range, USA. Geophys. Res. Lett. 29. https://doi.org/10.1029/2001GL014205 p. 26-1–26-4.

Willett, S.D., 1999. Orogeny and orography: The effects of erosion on the structure of mountain belts. J. Geophys. Res. Solid Earth 104, 28957–28981. https://doi.org/10.1029/1999JB900248.

Williams, C.A., Wadge, G., 1998. The effects of topography on magma chamber deformation models: application to Mt. Etna and radar interferometry. Geophys. Res. Lett. 25, 1549–1552. https://doi.org/10.1029/98GL01136.